

## Flexible aircraft flight dynamics and loads model identification from flight test data in unsteady conditions

Jurisson, A.; Eussen, Bart; de Visser, C.C.; De Breuker, R.

**Publication date**

2024

**Document Version**

Final published version

**Published in**

Aeroelasticity & Structural Dynamics in a Fast Changing World 17 – 21 June 2024, The Hague, The Netherlands

**Citation (APA)**

Jurisson, A., Eussen, B., de Visser, C. C., & De Breuker, R. (2024). Flexible aircraft flight dynamics and loads model identification from flight test data in unsteady conditions. In *Aeroelasticity & Structural Dynamics in a Fast Changing World 17 – 21 June 2024, The Hague, The Netherlands* Article IFASD 2024-198

**Important note**

To cite this publication, please use the final published version (if applicable). Please check the document version above.

**Copyright**

Other than for strictly personal use, it is not permitted to download, forward or distribute the text or part of it, without the consent of the author(s) and/or copyright holder(s), unless the work is under an open content license such as Creative Commons.

**Takedown policy**

Please contact us and provide details if you believe this document breaches copyrights. We will remove access to the work immediately and investigate your claim.

## **FLEXIBLE AIRCRAFT FLIGHT DYNAMICS IDENTIFICATION FROM FLIGHT TEST DATA IN UNSTEADY CONDITIONS**

**Andres Jürisson<sup>1</sup>, Bart Eussen<sup>1</sup>, Coen de Visser<sup>2</sup>, Roeland de Breuker<sup>2</sup>**

<sup>1</sup>Royal Netherlands Aerospace Centre  
Anthony Fokkerweg 2, 1059CM Amsterdam, The Netherlands  
Andres.Jurisson@nlr.nl  
Bart.Eussen@nlr.nl

<sup>2</sup>Delft University of Technology  
Kluyverweg 1, 2629HS Delft, The Netherlands  
c.c.devisser@tudelft.nl  
R.DeBreuker@tudelft.nl

**Keywords:** system identification, flight testing, unsteady aerodynamics, flight dynamics, aeroelasticity

**Abstract:** In this paper, a flight dynamics model was identified for a scaled Diana 2 glider aircraft that included the influences from its flexible structure and the delayed effects caused by unsteady aerodynamics. Flight tests were conducted to collect response measurements to various excitation manoeuvres. A method was developed to obtain the pole values for aerodynamic lag states from the flight test measurements. These poles characterise the delays in aerodynamic force and moment responses caused by unsteady aerodynamics and are necessary to be able to reconstruct the aerodynamic lag states. Ordinary least squares regression was applied to estimate the aerodynamic force and moment coefficients. The inclusion of structural modes and aerodynamic lag states led to improvements in the fitting accuracy, when compared to a rigid aircraft model with the largest improvement of 32% achieved for aircraft roll moment coefficient.

## 1 INTRODUCTION

In the pursuit of enhancing aircraft performance and reducing fuel consumption, modern aircraft designs are incorporating longer and more slender wings, along with the use of lighter materials. However, longer wingspans and lower structural stiffness often lead to a closer interaction between the aircraft's rigid-body responses and aeroelastic effects, primarily due to lower structural frequencies. Understanding this interaction accurately is crucial not only for ensuring the safety of the vehicle but also for developing high-fidelity flight simulators for pilot training, designing control laws to enhance aircraft performance, and alleviating the loads exerted on the aircraft.

System identification methods provide a way to obtain models that capture these effects from flight test measurements. While system identification methods for rigid aircraft are well established, limited reference literature is available specifically for identifying flexible aircraft, particularly using flight test data. Grauer [1] highlights the main challenges in flexible aircraft system identification, including the complexity of larger models, the necessity to excite a broad range of frequencies during flight tests, the requirement of numerous additional sensors, the lack of direct observability of modal states, and often used nonlinear methods that necessitate good starting values.

Previous studies have employed various identification methods for different aircraft models. For instance, Grauer and Boucher [1, 2] employed the equation-error approach and output-error approach in the frequency domain to identify the longitudinal dynamics models of the X-56A aircraft. Danowsky et al. [3] used prediction-error methods in the time domain to identify a scaled version of the X-56A aircraft. Silva [4] employed output-error methods in the time domain to identify the SB10 glider model. The mean-axis formulation by Waszak and Schmidt [5] is most commonly used to describe the flight dynamics of flexible aircraft together with quasi-steady aerodynamics, lumping all unsteady aerodynamic effects into the aeroelastic stability derivatives. However, these models may not accurately capture changes in response amplitudes and phase shifts caused by unsteady aerodynamic effects.

This paper presents a method for identifying flight dynamics models for flexible aircraft while considering unsteady aerodynamic effects. The paper introduces a method for determining the aerodynamic lag poles and reconstructing the aerodynamic lag states, which are core components in capturing unsteady effects. A full model, including both lateral and longitudinal dynamics, is determined for a scaled Diana 2 glider aircraft. The identification approach utilizes a two-step method, where measurements are first filtered using a previously developed approach that extends the flight path reconstruction method [6]. This step is then followed by an ordinary least square fitting process to estimate model parameters. This approach circumvents nonconvex optimization problems that depend on having good initial parameter values. The identified model is a gray-box model with physically meaningful parameters, providing insights into the aircraft's behaviour.

The structure of the paper is as follows. Section 2 provides a brief overview of aircraft unsteady aerodynamics modelling and proposes a method for reconstructing lag states from flight test response measurements. Section 3 presents an overview of the test aircraft and the conducted flight tests. Section 4 gives an overview of the model identification process and the derivation of the aerodynamic force and moment coefficients. Section 5 presents the identified model structures, including the estimation of aerodynamic lag state poles. Finally, Section 6 presents the summary and future developments.

## 2 THEORETICAL BACKGROUND

In this section, a brief overview of aeroelastic aircraft and unsteady aerodynamics modelling is presented, and a method for reconstructing lag states from flight test response measurements is proposed. To illustrate the proposed method, a typical section model is used for simplicity. A typical section is an aeroelastic model of a symmetric airfoil with heave and pitch degrees-of-freedom (DOF). Then, according to Theodorsen [7], the lift force and moment about the airfoil elastic axis can be described by circulatory and non-circulatory terms. These circulatory terms are frequency dependent and are related to the vorticity in the airflow. The Theodorsen function is used to describe the circulatory terms which models the amplitude and phase changes in unsteady aerodynamic forces relative to quasi-steady forces at different reduced frequencies. Reduced frequency, denoted by  $k$ , is defined in eq. 1, where  $\omega$  is the circular frequency,  $\bar{b}$  is the half-chord length, and  $V$  is the airspeed.

$$k = \frac{\omega \bar{b}}{V} \quad (1)$$

In Figure 1, the Theodorsen function is evaluated for varying reduced frequencies, and the changes in amplitude and phase are presented. As can be seen, the largest phase differences between unsteady and quasi-steady forces occur at reduced frequencies of around 0.15-0.3.

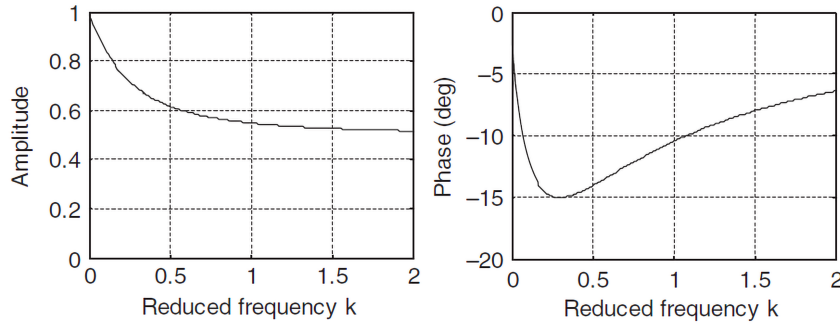


Figure 1: Theodorsen function amplitude and phase lag effects [8].

While the Theodorsen function describes the model in frequency domain, a time domain description can be obtained from Jones' approximation to Wagner's function [9] as presented in eq. 2 where  $\Psi_1 = 0.165$ ,  $\Psi_2 = 0.335$  and  $p_1 = -0.0455$ ,  $p_2 = -0.3$ .

$$\phi(t) = 1 - \Psi_1 e^{p_1 \frac{V}{\bar{b}} t} - \Psi_2 e^{p_2 \frac{V}{\bar{b}} t} \quad (2)$$

The dynamics of eq. 2 can also be represented using aerodynamics lag states as shown in eq. 3, which is more suitable format for state-space modelling.

$$\dot{x}_{lag} = p_i \frac{V}{\bar{b}} x_{lag} + u \quad (3)$$

Here  $u$  corresponds to the model DOF and  $x_{lag}$  is the corresponding state with delayed responses. In Figure 2, the effect of different pole values is illustrated with step responses when using the Diana 2 glider chord length and an airspeed of  $20m/s$ . As can be seen, more negative pole values lead to a smaller delay in the responses.

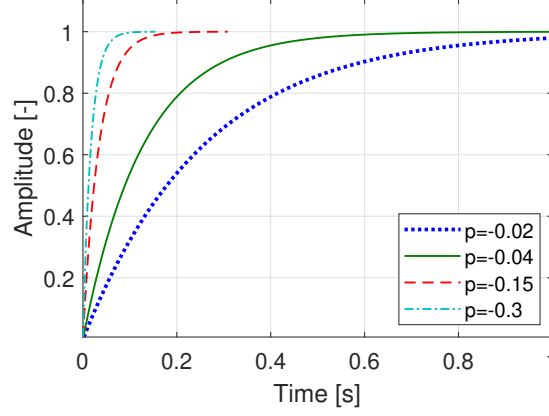


Figure 2: Lag pole effect on the lag state response.

These aerodynamic lag states are also used as part of rational function approximation (RFA), where the generalized forces  $Q(s)$  corresponding to a 3D frequency domain solution are fitted with aerodynamic matrices  $A_i$  as shown in eq. 4 to obtain a time domain approximation [8].

$$Q(s) = A_0 + A_1s + A_2s^2 + \sum_{i=1}^{N_{lag}} \frac{A_{2+i}s}{s + p_i \frac{V}{b}} \quad (4)$$

While the lag poles for the 2-DOF typical section are known and can be obtained from Jones' approximation, in the RFA fitting procedure they are additional variables for fitting the frequency domain solution. However, such a solution is not available when using flight test response measurements and measuring the lag states directly is also not possible. Therefore, an alternative way of determining the lag poles and lag states is required.

The proposed method for determining the lag pole values and reconstructing the lag states is first demonstrated using a 2-DOF typical section model. Derivation by Boutet and Dimitriadis [10] was followed to obtain a state-space model of the typical section as shown in eq. 5.

$$M_s \ddot{x} + K_s x = \bar{q} (A_2 \ddot{x} + A_1 \dot{x} + A_0 x + A_{lag} x_{lag}) \quad (5)$$

where  $x$  is the state vector with pitch and plunge DOF,  $M_s$  and  $K_s$  contain the structural mass and stiffness terms while  $A_0, A_1, A_2$  are the aerodynamic matrices and  $x_{lag}$  is a vector of aerodynamic lag states. Using this model, responses to different initial conditions were simulated and the pitch  $\theta$  and plunge  $h$  states together with lift force  $C_L$  and pitch moment  $C_m$  coefficients were recorded as shown in Figure 3. From these responses, the goal is to estimate the lag poles and reconstruct the lag states.

The lag state system inputs in the typical section case are the pitch angle and plunge states. Next, the lag states are reconstructed according to eq. 6 for varying pole values using the measured inputs. In the case of flight test measurements, also the changing airspeed needs to be accounted for during the reconstruction. Using the reconstructed lag states, correlation with the aerodynamic force and moment coefficients are determined for each pole value. A lag pole and the corresponding reconstructed lag state that results in a peak in correlation is then selected as a candidate for modelling.

$$x_{lag}(t_{k+1}) = (1 + p_i \frac{V(t_k)}{b}) \Delta t x_{lag}(t_k) + \Delta t u(t_k) \quad (6)$$

where  $\Delta t$  is the sampling time of the response measurements and  $t_k$  is the sample at time  $t$ .

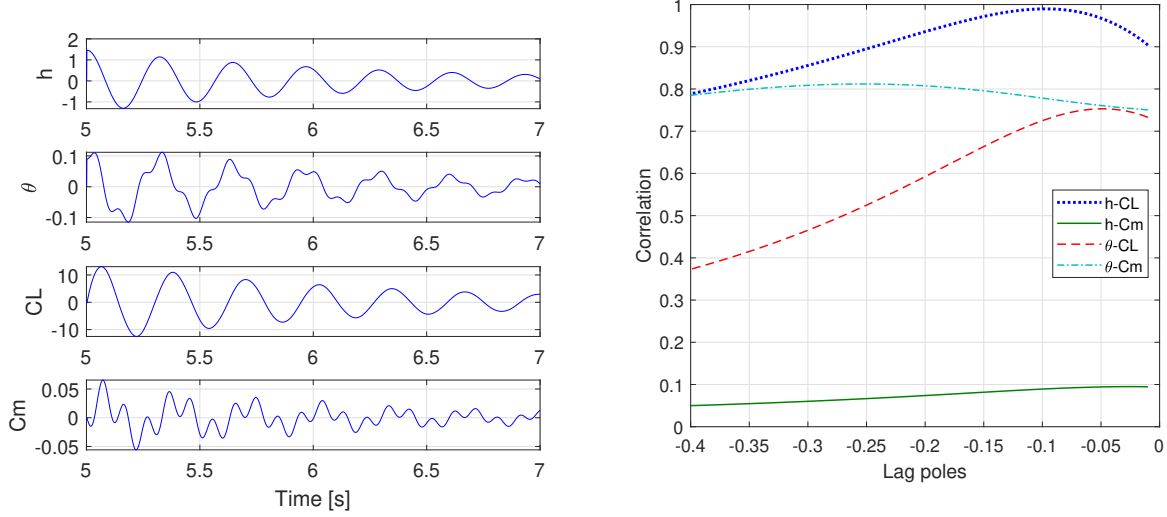


Figure 3: Typical section response to an initial condition. Figure 4: Lag state correlation with response signals for varying lag pole values.

In Figure 4 the correlation values for varying pole values are presented for different typical section input-response combinations. As the lag poles are varied between  $-0.01$  and  $-0.4$ , some input-response combinations exhibit clear peaks in correlation. Table 1 presents the pole values corresponding to the peaks in the presented correlation plots. As can be seen, the method is able to find estimates that are close to the true pole values of  $-0.0455$  and  $-0.3$ . There is also a peak corresponding to pole  $-0.1$ , which is not present in the typical section model. Therefore, all these candidate lag states need to be considered during modelling, where it can be determined which lag states lead to improvements in modelling accuracy and should be included in the model.

Table 1: Lag pole estimates determined from typical section responses.

Input	Response	Pole
h	CL	-0.1
h	Cm	-0.049
$\theta$	Cm	-0.255

### 3 TEST AIRCRAFT AND FLIGHT TESTING

A 1 to 3 scaled Diana 2 glider is used as the flight test platform for collecting the flight response measurements during this research. This is an unmanned aerial vehicle (UAV) with a weight of around 11 kilograms and high aspect ratio wings with a wingspan of 5 meters. The model has 2 ailerons and 1 flap on each wing and elevator and rudder in a T-tail configuration. There is also an electric propulsion system with folding propellers in the nose of the aircraft. The main technical parameters of the scaled glider are presented in Table 2 while an image of the glider is presented in Figure 5.

Table 2: Diana 2 model technical data.

Property	Value
Aspect ratio	24.3
Mass	10.7 kg
Mean aerodynamic chord	0.206 m
Wing area	$1.03 \text{ m}^2$
Wingspan	5.0 m



Figure 5: Diana 2 scaled glider [11].

#### 3.1 Instrumentation

To capture the responses of the aircraft and its structure, the glider is instrumented with numerous sensors placed across the entire aircraft. In total, 36 acceleration and rotational rate responses are measured using 3-axis ICM-20948 inertial measurement units (IMUs). In addition, the structural deformations and loads acting on the aircraft are measured using shear and bending strain gauges. In total, 21 strain responses are measured, with 9 responses from each wing and 3 from the tail. Furthermore, a 5-hole aeroprobe is used to measure the airspeed, angle of attack, and angle of sideslip. Aircraft position is determined using an RTK-GPS system, and control surface deflections are measured using magnetic rotary encoders. An overview of the sensors and their locations are illustrated in Figure 6.

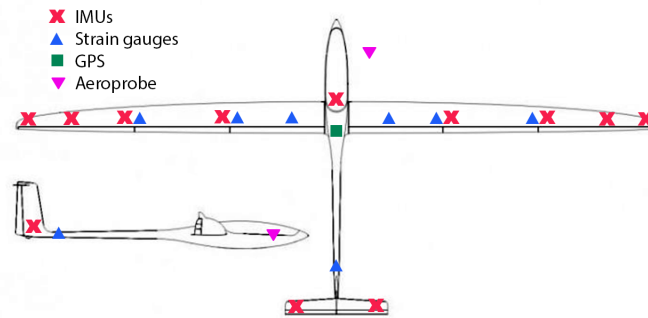


Figure 6: Diana 2 sensor placement overview.

For flying the aircraft, a differential aileron mixing law has been implemented based on manufacturer recommendations. The mixing law limits the maximum aileron upwards deflections to 100% for outer and 70% for middle aileron and downwards deflections 60% for outer and 50% for middle aileron. This way the outer and middle aileron movements were always linked during flight testing. Instead of using the individual control surface measurements for modelling, symmetric and asymmetric aileron signals are computed as shown in eq. 7 and eq. 8 with the individual right wing outer (RO) and left wing outer (LO) aileron deflection measurements. A

similar procedure was then followed for the middle ailerons and flaps.

$$\delta_a^{sym} = \frac{1}{2}(\delta_a^{RO} + \delta_a^{LO}) \quad (7)$$

$$\delta_a^{asym} = \frac{1}{2}(\delta_a^{RO} - \delta_a^{LO}) \quad (8)$$

This way, the symmetric aileron signal contains the averaged effect of the ailerons, while the asymmetric aileron signal contains the offset due to the mixing law deflecting ailerons more upwards.

### 3.2 Aircraft structural properties

A ground vibration test (GVT) was conducted using the integrated sensors to determine the modal parameters corresponding to the aircraft structure. This test was also used to validate the accuracy and sensitivity of the sensors in capturing the structural modes. Table 3 presents an overview of the first six structural modes, while detailed results can be found in [12].

Table 3: Overview of scaled Diana 2 structural modes.

Mode	Frequency [Hz]	Damping [-]	Description
1	7.42	2.88%	1st sym. wing bending
2	9.94	2.18%	Tail roll
3	13.82	2.72%	Vertical tail torsion
4	17.31	1.10%	2nd asym. wing bending
5	20.01	0.75%	1st inplane wing bending
6	21.19	2.47%	Fuselage bending out of sym. plane

In Figure 7 to Figure 10, the mode shapes for the first 4 modes are presented. The GVT was conducted using accelerometers, gyroscopes, and strain gauges; the resulting mode shapes include displacement, rotational, and strain modes. In these figures, the displacement corresponds to the displacement mode shapes. The arrows represent the rotational mode shapes and point in the resultant vector direction. Finally, the colours correspond to the strain mode shapes with blue marking compression and red tension.

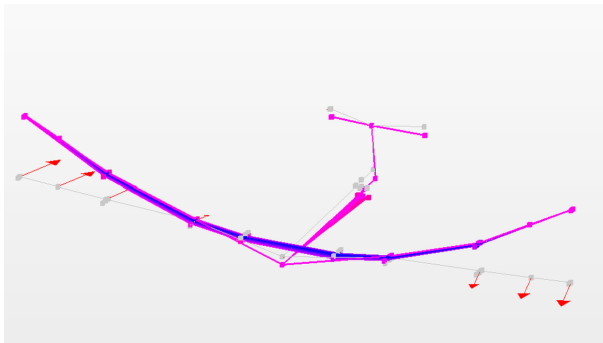


Figure 7: Mode 1 - 1st sym. wing bending.

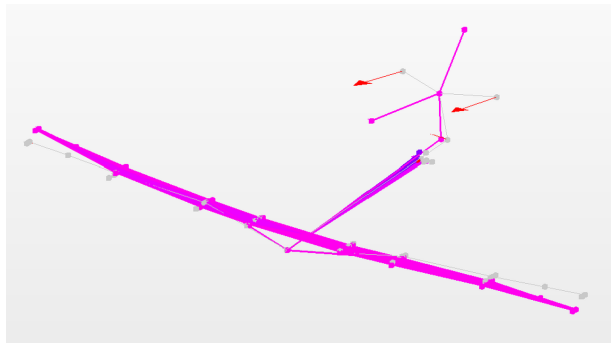


Figure 8: Mode 2 - tail rotation around x-axis.



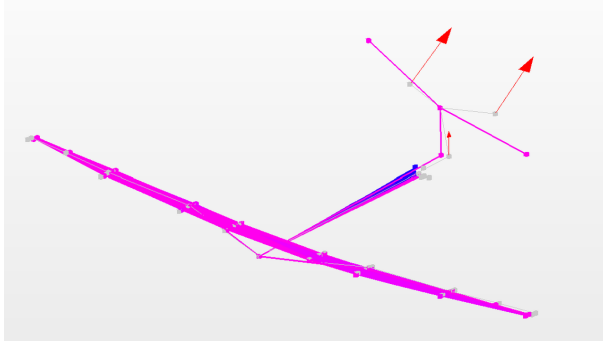


Figure 9: Mode 3 - tail rotation around z-axis.

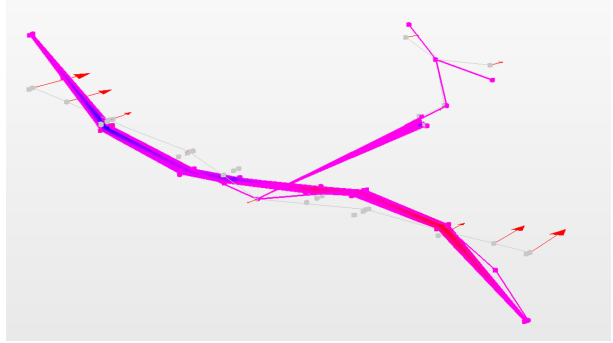


Figure 10: Mode 4 - 2nd asym. wing bending.

During the GVT, also the moment of inertia of the aircraft was estimated, which is presented in Table 4.

Table 4: Moment of inertia of scaled Diana 2 glider.

Inertia	Value [ $kgm^2$ ]
$I_x$	4.445
$I_y$	1.642
$I_z$	6.897
$I_{xz}$	0.332

### 3.3 Test manoeuvres

The flight test campaign was conducted at the airfield at the Netherlands Aerospace Centre premises in Marknesse, The Netherlands. In total, 9 flight tests were successfully recorded over 4 separate flight testing days. The flights were conducted by piloting the aircraft remotely by line-of-sight using an RC radio transmitter. First, a climb to a target altitude of around 150-200 meters was performed using the electric motor. Then the engine was turned off and the excitation manoeuvres were performed during the gliding part of the flight. The excitations were initiated from straight and level flight conditions at an airspeed between 20-25  $m/s$ . As seen from Figure 11, this places the first structural mode and control surfaces at a target reduced frequency condition of 0.15-0.3 where the phase shift is the largest as shown in Figure 1.

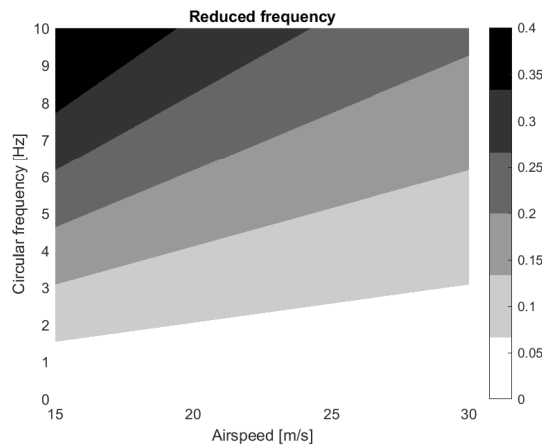


Figure 11: Reduced frequency for varying airspeeds and circular frequencies for the scaled Diana 2 glider.

Table 5 presents an overview of the conducted flight test manoeuvres. It shows what type of excitation was performed, on which control surface, and how many times it was repeated. As the manoeuvres were performed manually by the pilot, there were significant variations in excitation amplitudes and frequencies between each repetition. For the identification procedure, the test segments were randomly allocated into fitting and validation datasets, as presented in the table.

Table 5: Overview of conducted flight test manoeuvres.

Manoeuvre	Control surface				Data partitioning	
	Aileron	Elevator	Rudder	Combined	Fitting	Validation
Impulse	2	5	2	-	4	5
Doublet	8	9	5	-	12	10
3211	6	6	6	-	9	9
Freq. sweep	1	3	4	-	3	5
Combined	-	-	-	19	9	10
Total:	17	23	17	17	37	39

While more test manoeuvres were conducted, some needed to be excluded during post-processing as those segments had gaps with missing measurements for some sensors. After all response measurements were collected, they were resampled to a uniform 200 Hz sampling time, and a low-pass filter with a 60 Hz cutoff was applied.

## 4 FLEXIBLE AIRCRAFT MODEL IDENTIFICATION

The flexible aircraft model identification was conducted using the Two-Step Method (TSM) approach. The TSM approach separates the non-linear aerodynamic model identification problem into separate state estimation and parameter estimation problems.

### 4.1 State estimation

In the first step, an Extended Kalman filter is used to perform flight path reconstruction, where information from different sensor measurements is combined with the aircraft's rigid-body kinematic equations to obtain a filtered estimate for the aircraft's states. These measurements include the aircraft's rigid-body responses in terms of acceleration, rotational rate, position, attitude, airspeed, and aerodynamic flow angles. These rigid aircraft kinematic equations were extended for a flexible aircraft by also including structural dynamics. This allowed to obtain estimates for the modal amplitude and velocity states by incorporating additional measurements from accelerometers, gyroscopes, and strain gauges placed across the aircraft's structure together with structural mode shapes obtained during the GVT. A more thorough overview of this method is presented by Jurisson et al. [6].

### 4.2 Derivation of aerodynamic coefficients

Using the filtered signals of the aircraft's states, it was then possible to calculate the aircraft's aerodynamic force and moment coefficients. The equations of motion for an elastic aircraft are most often represented using the mean-axis formulation as it closely resembles conventional flight dynamics equations [2, 5]. The translation of the aircraft center of mass can be described using eq. 9 to eq. 11.

$$\bar{q}SC_X = mA_x = m\dot{u} + m(qw - rv) + mg \sin \theta \quad (9)$$

$$\bar{q}SC_Y = mA_y = m\dot{v} + m(ru - pw) - mg \cos \theta \sin \phi \quad (10)$$

$$\bar{q}SC_Z = mA_z = m\dot{w} + m(pv - qu) - mg \cos \theta \cos \phi \quad (11)$$

The force coefficients  $C_X, C_Y, C_Z$  can be calculated from the  $A_x, A_y, A_z$  acceleration measurements using the aircraft mass  $m$ , wing area  $S$  and the dynamic pressure  $\bar{q}$ . By applying an axis transformation using the angle of attack  $\alpha$ , the lift  $C_L$  and drag  $C_D$  coefficients can be determined.

$$C_L = C_X \sin \alpha - C_Z \cos \alpha \quad (12)$$

$$C_D = -C_X \cos \alpha - C_Z \sin \alpha \quad (13)$$

The rotation of the aircraft's mean-axis frame with respect to the inertial frame is stated by eq. 14 to eq. 16. Similarly, the moment coefficients  $C_l, C_m, C_n$  can be calculated from angular rates  $p, q, r$  and angular accelerations  $\dot{p}, \dot{q}, \dot{r}$  using the aircraft's mass moment of inertia, wingspan  $b$  and mean chord  $\bar{c}$  [13]. The angular accelerations  $\dot{p}, \dot{q}, \dot{r}$  were determined using numerical differentiation of the angular rates.

$$\frac{\bar{q}Sb}{I_x} C_l^{CG} = \dot{p} - \frac{I_{xz}}{I_x} \dot{r} + \frac{I_z - I_y}{I_x} qr - \frac{I_{xz}}{I_x} qp \quad (14)$$

$$\frac{\bar{q}S\bar{c}}{I_y} C_m^{CG} = \dot{q} - \frac{I_x - I_z}{I_y} pr + \frac{I_{xz}}{I_y} (p^2 - r^2) \quad (15)$$

$$\frac{\bar{q}Sb}{I_z} C_n^{CG} = \dot{r} - \frac{I_{xz}}{I_z} \dot{p} + \frac{I_y - I_x}{I_z} pq + \frac{I_{xz}}{I_z} qr \quad (16)$$

The moment coefficients around the aerodynamic center reference point can then be found according to eq. 17 to 19 where  $\Delta X_{CG}$ ,  $\Delta Y_{CG}$ ,  $\Delta Z_{CG}$  represent the distance from aircraft center of gravity to the aerodynamic center [13].

$$C_l^{AC} = C_l^{CG} - C_Z \frac{\Delta Y_{CG}}{b} + C_Y \frac{\Delta Z_{CG}}{b} \quad (17)$$

$$C_m^{AC} = C_m^{CG} - C_X \frac{\Delta Z_{CG}}{\bar{c}} + C_Z \frac{\Delta X_{CG}}{\bar{c}} \quad (18)$$

$$C_n^{AC} = C_n^{CG} - C_Y \frac{\Delta X_{CG}}{b} + C_X \frac{\Delta Y_{CG}}{b} \quad (19)$$

The flexible aircraft's structural deformations are represented as linear combinations of vibration modes such as the ones presented in Sec. 3.2. For each structural vibration mode the dynamics are described by eq. 20, where  $\eta_i$  is the modal amplitude,  $m_i$  is the modal mass,  $\omega_i$  is the modal frequency and  $\xi_i$  the damping ratio while  $C_{Q_i}$  corresponds to the generalized force coefficient. The modal mass, frequency, and damping parameters were estimated during the GVT, while the modal accelerations  $\ddot{\eta}_i$  were obtained by numerical differentiation of the modal velocities  $\dot{\eta}_i$  obtained from state estimation.

$$\frac{\bar{q}S\bar{c}}{m_i} C_{Q_i} = \ddot{\eta}_i + 2\xi_i\omega_i\dot{\eta}_i + \omega_i^2\eta_i \quad (20)$$

### 4.3 Parameter estimation

By first performing a non-linear state estimation process, it is then possible to apply linear regression techniques for the parameter estimation step. This is in contrast to an output-error parameter estimation approach, where the model parameters are estimated in a single non-linear optimization process, which requires an initial guess for all parameters and does not guarantee a globally optimal solution.

In order to model the previously derived aerodynamic force and moment coefficients, Ordinary Least Squares (OLS) regression was applied. These derived aerodynamic coefficients are the dependent variables to be fitted, and they are assumed to contain errors that are zero-mean and have constant covariance, as shown in eq. 22.

$$\mathbf{z} = \mathbf{y} + \mathbf{v} \quad (21)$$

$$E[\mathbf{v}] = 0, \quad E[\mathbf{v}\mathbf{v}^T] = \sigma^2\mathbf{I} \quad (22)$$

where  $\mathbf{z}$  is the measurement vector,  $\mathbf{y}$  is the true value of the dependent variable and  $\mathbf{v}$  is the measurement error. It is then assumed that the dependent variable can be modeled as a linear combination of independent variables, as shown in eq. 23.

$$\mathbf{y} = \mathbf{X}\boldsymbol{\theta} \quad (23)$$

where  $\mathbf{X}$  is the regression matrix containing the independent variables and  $\boldsymbol{\theta}$  is the parameter vector to be estimated. The cost function for the OLS and the parameter estimate vector that results in an optimal solution is presented in eq. 24

$$J = \frac{1}{2}[\mathbf{z} - \mathbf{X}\boldsymbol{\theta}]^T[\mathbf{z} - \mathbf{X}\boldsymbol{\theta}], \quad \hat{\boldsymbol{\theta}} = (\mathbf{X}^T\mathbf{X})^{-1}\mathbf{X}^T\mathbf{z} \quad (24)$$

Multiple different metrics are used to help evaluate the model fitting results. The first metric is the commonly used coefficient of determination  $R^2$ , which measures the proportion of the variation in the dependent variable that is predictable from the independent variables.

$$R^2 = 1 - \frac{\sum_{k=1}^N v(k)^2}{\sum_{k=1}^N (z(k) - \hat{z}(k))^2} \quad (25)$$

Next is the Root Mean Square error, which is normalized by the difference between the maximum and minimum values of the variable being estimated.

$$RMS_{rel} = \frac{\sqrt{\frac{1}{N} \sum_{k=1}^N v(k)^2}}{|\max(z) - \min(z)|} \quad (26)$$

Finally, Theil's inequality coefficient (TIC) is a statistic that relates to the correlation between two time series, with values close to 0 indicating perfect fit and values close to 1 indicating maximum inequality. For reference, a TIC value around 0.25-0.3 can be considered a good agreement between the measured and predicted time series [13].

$$TIC = \frac{\sqrt{\frac{1}{N} \sum_{k=1}^N (y_i(k) - \hat{y}_i(k))^2}}{\sqrt{\frac{1}{N} \sum_{k=1}^N (y_i(k))^2 + \frac{1}{N} \sum_{k=1}^N (\hat{y}_i(k))^2}} \quad (27)$$

## 5 IDENTIFIED FLIGHT DYNAMICS MODELS

In this section, the models for the aircraft aerodynamic force and moment coefficients are identified. To fit these coefficients, linear models are used based on aircraft's rigid body states such as aerodynamic angles ( $\alpha, \beta$ ), rotational rates ( $p, q, r$ ) and control surface angles ( $\delta_e, \delta_r, \delta_a^{sym}, \delta_a^{asym}$ ) but also structural states ( $\eta_i, \dot{\eta}_i$ ) and aerodynamic lag states ( $x_{lag}$ ). While the states related to aircraft rigid body motion and structural dynamics were estimated during the state estimation step, it is necessary to estimate the aerodynamic lag poles and reconstruct the lag states before model identification can be performed.

### 5.1 Aerodynamic lag pole estimation

The aerodynamic lag states are related to the delays in the aircraft's responses due to unsteady aerodynamics. This means that the forces and moments take some time to react to changes instead of being instantaneous, as in models with steady aerodynamics. These lag states are driven by changes in the aircraft's attitude, control surface deflection, or structural deformations. To estimate the lag poles, the procedure described in Sec. 2 was applied to all individual flight test manoeuvres by taking the changes in the aircraft states as input signals and correlating them with the aircraft's aerodynamic coefficient signals for varying pole values. By repeating the estimation procedure for each flight test manoeuvre, a distribution of estimated lag poles was obtained, which are presented in Figure 12.

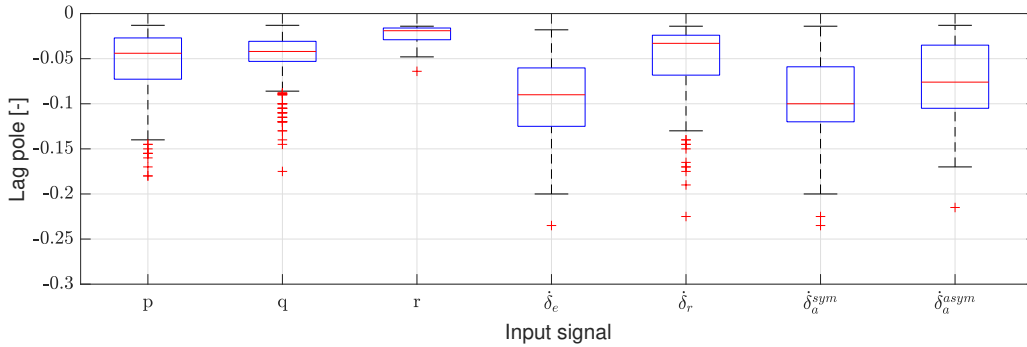


Figure 12: Estimated lag pole distributions for Diana 2.

In these box plots, the red lines represent the median value of the estimated poles, which are also shown in Table 6. The edges of the boxes indicate the 25th and 75th percentiles. As can be seen, most of the estimated lag poles are distributed close to  $-0.0455$ , which is Jones' approximation value for a 2D wing. This shows that the high aspect ratio wings of a glider aircraft correspond well to a 2D case. The lag pole estimate for the elevator  $\delta_e$  is  $-0.09$ . When accounting for the chord length of the horizontal tail, which is approximately half the size of the wing, an equivalent value close to  $-0.045$  would be again obtained. The poles for the ailerons  $\delta_a^{sym}, \delta_a^{asym}$  are  $-0.1$  and  $-0.076$ , but here the difference from the Jones' value is assumed to be due to the mixing law on the ailerons.

Table 6: Aerodynamic lag states and pole estimates.

Lag state	$x_{lag}^p$	$x_{lag}^q$	$x_{lag}^r$	$x_{lag}^{\delta_e}$	$x_{lag}^{\delta_r}$	$x_{lag}^{\delta_a^{sym}}$	$x_{lag}^{\delta_a^{asym}}$
Input	p	q	r	$\delta_e$	$\delta_r$	$\delta_a^{sym}$	$\delta_a^{asym}$
Pole	-0.044	-0.042	-0.019	-0.090	-0.033	-0.100	-0.076

In Figure 12, the red '+' markers represent the outliers that are further away from the median values. While most estimated pole values lie within the boxes, these outliers could also correspond to faster poles such as the -0.3 pole in Jones' approximation. However, consistent detection of such a pole can be difficult for the Diana 2 glider due to the very small delay. For reference, when flying the Diana 2 glider at 20.0m/s, pole values of  $-0.0455$  and  $-0.3$  represent a delay of around 0.5s and 0.07s, respectively.

With the lag state poles estimated, it was possible to reconstruct the lag states using the input signals and the measured airspeed according to eq. 6.

## 5.2 Flight dynamics model

After reconstructing the aerodynamic lag states and including them in the regression matrix together with the aircraft's rigid body states, control surface angles and structural modal states, it was possible to identify the flight dynamics model of the scaled Diana 2 glider. Different sets of regressors were used to model each coefficient. The independent variables in these sets were determined by performing the fitting using only a single variable and keeping only the variables in the set that individually showed an improvement in the fitting. With the resulting regressor sets, the optimal model structure was determined by evaluating all the possible combinations of regressors in the model for varying model sizes and choosing the best-performing structure according to the validation dataset. This was possible due to the low computational demand of the OLS. Alternatively, methods like stepwise regression could also be used to determine the model structure [14].

Two flight dynamics models were identified for the Diana 2. A "rigid" aircraft model that consists only of regressors related to the aircraft's rigid body responses and control surface deflections, and a "flexible" model that also includes the structural states and aerodynamic lags. The identified model structures for both cases are as follows:

$$C_D^{rigid} = C_{D_0} + C_{D_\alpha} \alpha + C_{D_{\alpha^2}} \alpha^2 \quad (28)$$

$$C_D^{flex} = C_{D_0} + C_{D_\alpha} \alpha + C_{D_{\alpha^2}} \alpha^2 \quad (29)$$

$$C_Y^{rigid} = C_{Y_0} + C_{Y_\beta} \beta + C_{Y_r} \frac{rb}{2V} + C_{Y_{\delta_r}} \delta_r \quad (30)$$

$$C_Y^{flex} = C_{Y_0} + C_{Y_\beta} \beta + C_{Y_{x_{lag}^r}} x_{lag}^r + C_{Y_{x_{lag}^{\delta_r}}} x_{lag}^{\delta_r} + C_{Y_{\eta_2}} \eta_2 \quad (31)$$

$$C_L^{rigid} = C_{L_0} + C_{L_\alpha} \alpha + C_{L_q} \frac{q\bar{c}}{2V} + C_{L_{\delta_e}} \delta_e \quad (32)$$

$$C_L^{flex} = C_{L_0} + C_{L_\alpha} \alpha + C_{L_{x_{lag}^{\delta_e}}} x_{lag}^{\delta_e} + C_{L_{\eta_1}} \eta_1 + C_{L_{\eta_5}} \eta_5 \quad (33)$$

$$C_l^{rigid} = C_{l_0} + C_{l_\beta} \beta + C_{l_p} \frac{pb}{2V} + C_{l_q} \frac{q\bar{c}}{2V} + C_{l_r} \frac{rb}{2V} + C_{l_{\delta_e}} \delta_e + C_{l_{\delta_a^{sym}}} \delta_a^{sym} \quad (34)$$

$$C_l^{flex} = C_{l_0} + C_{l_{x_{lag}^p}} x_{lag}^p + C_{l_{\delta_a^{sym}}} x_{lag}^{\delta_a^{sym}} \quad (35)$$

$$C_m^{rigid} = C_{m_0} + C_{m_\alpha} \alpha + C_{m_q} \frac{q\bar{c}}{2V} + C_{m_{\delta_e}} \delta_e \quad (36)$$

$$C_m^{flex} = C_{m_0} + C_{m_\alpha} \alpha + C_{m_{x_{lag}^q}} x_{lag}^q + C_{m_{\delta_e}} x_{lag}^{\delta_e} \quad (37)$$

$$C_n^{rigid} = C_{n_0} + C_{n_\beta} \beta + C_{n_p} \frac{pb}{2V} + C_{n_r} \frac{rb}{2V} + C_{n_{\delta_r}} \delta_r \quad (38)$$

$$C_n^{flex} = C_{n_0} + C_{n_{\delta_a^{sym}}} \delta_a^{sym} + C_{n_{x_{lag}^r}} x_{lag}^r + C_{n_{\delta_r}} x_{lag}^{\delta_r} + C_{n_{\eta_2}} \eta_2 \quad (39)$$

When determining the model structures, the priority was to keep the models concise with as few parameters as possible while still achieving a good fit. Table 7 presents the fitting results for the aircraft aerodynamic force and moment coefficients.

Table 7: Flight dynamics coefficient fitting results.

Coefficient	$R^2$	TIC	$RMS_{rel}$
$C_D$ rigid	81.79%	0.128	2.73%
$C_D$ flexible	81.79%	0.128	2.73%
$C_Y$ rigid	79.65%	0.233	3.56%
$C_Y$ flexible	92.74%	0.134	2.13%
$C_L$ rigid	84.88%	0.091	3.39%
$C_L$ flexible	89.36%	0.078	2.84%
$C_l$ rigid	51.54%	0.436	3.90%
$C_l$ flexible	83.99%	0.213	2.24%
$C_m$ rigid	81.75%	0.157	3.13%
$C_m$ flexible	91.18%	0.111	2.17%
$C_n$ rigid	78.45%	0.258	3.99%
$C_n$ flexible	91.51%	0.153	2.50%

As can be seen, including structural modes and aerodynamic lag states in the flexible aircraft model improved the fitting results. The only exception was the drag coefficient  $C_D$ , where additional parameters did not lead to significant improvements. The largest improvement was seen for the aircraft rolling moment coefficient  $C_l$ . With the rigid model, only a 51%  $R^2$  fit was achieved even when including nearly all the regressors available for the rigid model. A 32% improvement in  $R^2$  was obtained with the flexible model that included only the aerodynamic lag state related to the roll rate and symmetric aileron input in addition to the constant term  $C_{l_0}$ . This really emphasized the importance of including aerodynamic lag states in the model.

Close to or over 10% improvement was also achieved for the side force  $C_Y$ , pitching moment  $C_m$ , and yaw moment  $C_n$  coefficients, while lift  $C_L$  coefficient improved by 4.5%. With the side force and pitching moment coefficients, it can be seen that the model structures are nearly the same between the rigid and flexible models and that the improvements are obtained by using the aerodynamic lag states corresponding to the regressors in the rigid model.



In addition to the aerodynamic lag states, also the first  $\eta_1$ , second  $\eta_2$ , and fifth  $\eta_5$  structural modes were included in the flexible model. The first wing bending mode had the largest influence on the lift response, while the tail roll mode had the largest influence on the side force and yaw moment coefficients.

To illustrate the differences between the rigid and flexible model, fitting results are presented for three manoeuvres from the validation set during which all control surfaces were simultaneously excited. This allows to observe responses and fitting results on all axes simultaneously. In Figure 13, the control surface inputs and aerodynamic force and moment measurement responses are presented together with the rigid and flexible model predictions.

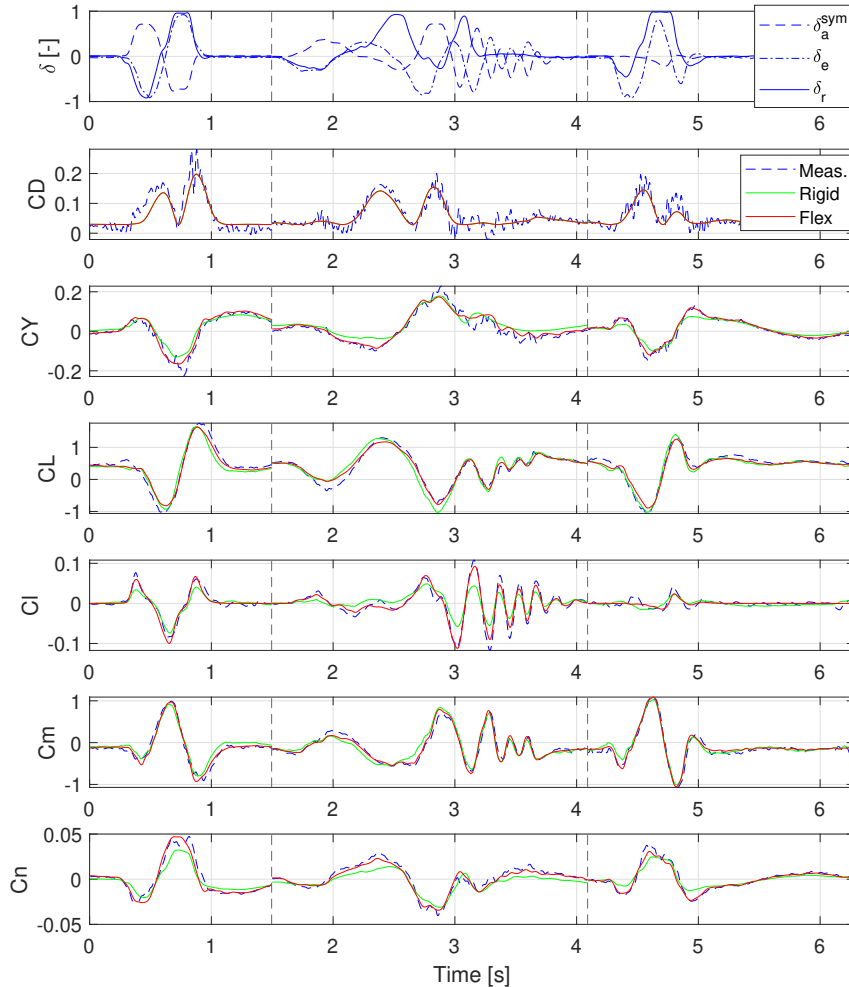


Figure 13: Aerodynamic force and moment coefficient fitting comparison.

It can be seen that both the rigid and flexible model capture the dynamic responses of the scaled Diana 2 glider well, with the flexible model achieving improved predictions. Only for the rolling coefficient is there a large difference in the response amplitudes predicted by the rigid model.

## 6 SUMMARY AND FUTURE WORK

In this paper, the flight dynamics model was identified for a scaled Diana 2 glider aircraft, which included the effects of its flexible structure and unsteady aerodynamics. A method was developed to determine the pole values and reconstruct the aerodynamic lag states, which capture the response delays caused by unsteady aerodynamics. Applying this method to flight test measurements allowed to successfully obtain lag poles that are close to values predicted by theory for 2D aeroelastic airfoils. Ordinary least squares regression was employed to estimate the aerodynamic force and moment coefficients from the flight test measurements for two models: one assuming the aircraft is rigid and another considering the flexible structure and unsteady aerodynamic forces. When structural and aerodynamic lag states were included in the flexible model, improved fitting accuracy was observed for all coefficients except for the drag coefficient. The most significant improvement of 32% was achieved for the roll moment coefficient fitting by including aerodynamic lags related to the roll rate and aileron deflections. Given these promising results, future research will expand the models to identify the generalized force coefficients associated with the included structural modes. Additionally, simulation validation will be conducted to compare and validate the simulated responses predicted by the models with the actual flight response measurements.

## 7 REFERENCES

- [1] Grauer, J. A. and Boucher, M. J. (2018). Real-time parameter estimation for flexible aircraft. *AIAA Atmospheric Flight Mechanics Conference*, AIAA, p. 25. doi:10.2514/6.2018-3155.
- [2] Grauer, J. A. and Boucher, M. J. (2018). *Output Measurement Equations for Flexible Aircraft Flight Dynamics*. TM-2018-220102. NASA Langley Research Center.
- [3] Danowsky, B. P., Schmidt, D. K., Schmidt, D. K., et al. (2017). Control-oriented system and parameter identification of a small flexible flying-wing aircraft. *AIAA Atmospheric Flight Mechanics Conference*, American Institute of Aeronautics and Astronautics, p. 25. doi:10.2514/6.2017-1394.
- [4] de Oliveira Silva, B. G. (2018). *System Identification of Flexible Aircraft in Time Domain*. Ph.D. thesis, Technical University of Braunschweig.
- [5] Waszak, M. R. and Schmidt, D. K. (1988). Flight dynamics of aeroelastic vehicles. *Journal of Aircraft*, 25(6), 563–571. ISSN 0021-8669. doi:10.2514/3.45623.
- [6] Jurisson, A., Eussen, B., de Visser, C. C., et al. (2023). Flight path reconstruction filter extension for tracking flexible aircraft modal amplitudes and velocities. In *AIAA Scitech 2023 Forum*. American Institute of Aeronautics and Astronautics, p. 13. doi:10.2514/6.2023-0626.
- [7] Theodorsen, T. (1949). General theory of aerodynamic instability and the mechanism of flutter. Tech. Rep. TR-496, NACA.
- [8] Wright, J. R. and Cooper, J. E. (2014). *Introduction to Aircraft Aeroelasticity and Loads*. Wiley. ISBN 9781118700440. doi:10.1002/9781118700440.
- [9] Jones, R. T. (1938). Operational Treatment of the Nonuniform-Lift Theory in Airplane Dynamics. Tech. Rep. NACA TN 667, NACA.
- [10] Boutet, J. and Dimitriadis, G. (2018). Unsteady lifting line theory using the wagner function for the aerodynamic and aeroelastic modeling of 3d wings. *Aerospace*, 5, 92. ISSN 22264310. doi:10.3390/aerospace5030092.
- [11] Jurisson, A., de Breuker, R., de Visser, C., et al. (2022). Aeroservoelastic flight testing platform development for system identification. In *AIAA Scitech 2022 Forum*. AIAA SciTech, American Institute of Aeronautics and Astronautics, p. 13. doi:10.2514/6.2022-2169.
- [12] Jurisson, A., Timmermans, H., Eussen, B., et al. (2022). Ground vibration testing and fem model updating of scaled diana 2 glider model using accelerometer, gyro and strain measurements. *International Forum on Aeroelasticity and Structural Dynamics*, IFASD, p. 10.
- [13] Jategaonkar, R. V. (2006). *Flight Vehicle System Identification: A Time Domain Methodology*, vol. 216 of *Progress in Astronautics and Aeronautics*. American Institute of Aeronautics and Astronautics. ISBN 1563478366.
- [14] Klein, V., Batterson, J. G., and Murphy, P. C. (1983). Airplane model structure determination from flight data. *Journal of Aircraft*, 20(5), 469–474. doi:10.2514/3.44895.

**COPYRIGHT STATEMENT**

The authors confirm that they, and/or their company or organisation, hold copyright on all of the original material included in this paper. The authors also confirm that they have obtained permission from the copyright holder of any third-party material included in this paper to publish it as part of their paper. The authors confirm that they give permission, or have obtained permission from the copyright holder of this paper, for the publication and public distribution of this paper as part of the IFASD 2024 proceedings or as individual off-prints from the proceedings.